30th NENE 2021
September 6 - 9
BLED-SLOVENIA
International Conference Nuclear Energy for New Europe

Nano-Oxides Precipitation Kinetics of Ferritic and Ferritic / Martensitic Oxide Dispersion Strengthened Steels

Gabriel Spartacus [a], Joël Malaplate [a],

[a] CEA Saclay, DEN/DMN/SRMA, 91191 Gif-sur-Yvette Cedex, France

spartac@kth.se, joel.malaplate@cea.fr

Frédéric De Geuser [b], Isabelle Mouton [a], Denis Sornin [a], Alexis Deschamps [b]

[a] CEA Saclay, DEN/DMN/SRMA, 91191 Gif-sur-Yvette Cedex, France

[b] SIMAP, Grenoble INP – CNRS – UJF, 1130 rue de la Piscine BP 75, 38402 Saint Martin d'Hères Cedex, France.

frederic.de-geuser@grenoble-inp.fr, isabelle.mouton@cea.fr, denis.sornin@cea.fr, alexis.deschamps@grenoble-inp.fr,

ABSTRACT

Oxide Dispersion Strengthened (ODS) steels are candidates materials to be used in nuclear fusion and 4th generation fission power plants. They are processed by powder metallurgy, following a Mechanical Alloying (MA) where Fe-Cr powder is mixed with 0.3 %wt Y_2O_3 and 0.3 %wt TiH_2 powders resulting in an as-MA powder where Y, Ti and O are dissolved into the Fe-Cr matrix. The as-MA powder is then consolidated at 1100°C by Hot Extrusion (HE) or Hot Isostatic Pressing (HIP), where the Y-Ti-O nano-oxide precipitation occurs. In this study, two grades of ODS steels are studied: a Fe-14Cr ferritic ODS, with higher corrosion resistance but non-isotropic mechanical properties when processed by HE; and a Fe-9Cr Ferritic / Martensitic (F/M) ODS, which exhibits a matrix $\alpha \rightarrow \gamma$ phase transformation around 950 °C resulting in a more isotropic microstructure (and then mechanical properties) after HE but a lower corrosion resistance. This work demonstrates the influence of the phase transformation of the F/M ODS steels on the precipitation kinetics, showing an increase of the nano-oxides growth rate after the $\alpha \rightarrow \gamma$ matrix transformation, resulting in a nano-oxide size two times bigger than ferritic ODS steels, thanks to in-situ Small Angle X-ray Scattering (SAXS) measurements up to 1100 °C. Very small clusters (~1 nm size) containing at least Y and O had been observed at the as-MA stage of both ODS grades. The comparison between SAXS and Atom Probe Tomography (APT) data allows to determine that the nano-oxides stoichiometry and structure stabilize at roughly ~1000 °C, for both alloys.

1 INTRODUCTION

Oxide Dispersion Strengthened (ODS) steels with a Fe-Cr matrix are of great interest in the development of future generation of nuclear power plants (fission and fusion). In the context of nuclear fusion power plants, ODS steels are excellent candidates to be used as cladding tubes for sodium-cooled fast neutron reactors of Gen. IV nuclear power plants [1]. Indeed, their ferritic matrix allows to achieve high resistance to swelling under irradiation, while the nano-oxides dispersion ensures a good creep resistance and acts as trapping sites from the He bubbles produced by transmutation under neutron irradiation [2]–[5]. ODS steels include a high density of Y-Ti-O precipitates of a few nm introduced by powder metallurgy, providing the main

contribution to the ODS steels strength [6]. During the process, a Fe-Cr atomized powder is milled together with a Y_2O_3 and a TiH_2 powders during a Mechanical Alloying (MA) stage. As-MA powder is then generally consolidated at ~1100°C by Hot Extrusion (HE) or Hot Isostatic Pressing (HIP).

Ferritic / Martensitic (F/M) grades (with lower Cr content than purely ferritic grades) demonstrate an enhanced formability during the fabrication process, especially when HE is applied, at the expense of the corrosion resistance (due to lower Cr content) [7]. The formability increase is linked to the phase transformation: ferrite (α) → austenite (γ) occurring at ~950°C, which results into a much lower texture and a more equiaxed grain shape after the process [8]. Yet, the nano-oxides population in F/M grades is known to be of greater size and lower density (approximately by a factor of 2 [9]). This change in the nano-oxides size is expected to originate from the α → γ phase transformation, on the basis of the post-thermal treatment results [10], [11]. However, at our knowledge, this hypothesis had never been demonstrated due to the difficulty of performing a direct observation. Indeed, due to their complex initial microstructure (as-MA), very small precipitates and their powder form, a few experimental data is currently available to describe the full precipitation kinetics (from as-MA to 1100°C, the industrial consolidation temperature), for either ferritic or F/M steels. Such data would be of first interest to the optimisation of the fabrication process as well as the numerical modelisation of the precipitation kinetics. Therefore, this article will present in- and ex-situ experimental measurements of the precipitation kinetics and chemical evolution of the nano-oxides comparing a purely ferritic and a F/M ODS steel grades through a thermal treatment representative to the HE industrial process.

2 MATERIALS AND METHODS

Two ODS steel grades of Fe-14Cr-1W and Fe-9Cr-1W were prepared by attrition milling for 10 hours at 440 rpm speed in a high purity Ar atmosphere of a Fe-Cr atomized powder with 0.3 %wt of Y_2O_3 and 0.3 %wt of TiH_2 powders. The ball-over-powder ratio during milling was approximately 0.067 and all the milling were performed at the LTMEx laboratory within the CEA research centre. Consolidation of the ODS as-MA powders was performed by HE or Cold Pressing (CP). During HE, the as-MA powder is sealed into a low-C can and outgazed at around 400°C. The can is then heated at ~ 40°C/min until 1100°C followed by 45 min isothermal before air cooling. In order to relief the residual stress induced by HE, an additional thermal treatment of 1050°C for 1h is apply, followed by air cooling. CP specimens were prepared in order to have dense specimen at the as-MA stage that could be used to investigate the precipitation kinetics of the nano-oxides in-situ and ex-situ all along the thermal treatment up to 1100°C. During the process, the as-MA powder is places into a low-C cladding and cold pressed under ~ 3 GPa to achieve a disk of a few millimetres. Specimens will therefore be denominated as CP-14Cr, HE-14Cr for the Fe-14Cr-1W ODS and CP-9Cr, HE-9Cr for the Fe-9Cr-1W ODS that respectively followed CP and HE.

Differential Scanning Calorimetry (DSC) was applied on a Fe-9Cr-1W as-MA ODS powder with an heating ramp at 10 °C/min in order to determine the temperatures of the start and full α → γ transformation (denominated Ac1 and Ac3 respectively).

Small Angle X-ray Scattering (SAXS) were performed during in-situ thermal treatment (heating ramp at 30 °C/min up to 1100 °C followed by 1h isothermal) at the ESRF synchrotron on the D2AM-BM02 beamline. Ex-situ measurements were also performed using a laboratory source at the SIMaP laboratory using a rotating Mo anode (generating an X-Ray energy of 17.45 keV). These experiments allow to monitor the mean radius of the nano-oxides R_m and the product of the electronic contrast between the matrix and the nano-oxides times their volume fraction $\Delta\rho^2 \times f_v$ from a model fitting method detailed in [12].

At the ESRF, the X-Ray beam energy during the measurements were shifted every 5 measurements of the specimen (on a 2D detector) and 1 measurement of the transmission between 16.829 keV and 17.009 keV in order to evaluate the anomalous effect at the Y K-edge (17.0384 keV), taking into account a counting time of 10 seconds. Anomalous SAXS (ASAXS) was analysed thanks to the evaluation of the anomalous factor following the method proposed by Dumont et al. [13], but will only be qualitatively analysed in the present manuscript. After acquisition, the 2D scattering patterns were azimuthally integrated, background subtracted and normalized from incident intensity, specimen thickness and transmission as well as solid angle of the detector. The SAXS intensity curves were then reduced into absolute unit thanks to a glassy carbon sample taken as a secondary standard.

Atom Probe Tomography (APT) was performed at several stages of the interrupted thermal treatment on CP-14Cr and CP-9Cr specimens using a LEAP 4000X HR in laser mode. APT allows to reconstruct in 3 dimensions the position and the nature of the atoms within a small evaporated volume of the materials. Prior to APT, samples were prepared by a FEI Dual Beam Hélios nanolab 650 Focused Ion Beam (FIB). During APT measurement, a laser energy of 60 nJ with a frequency varying between 125 and 200 kHz (tuned depending on the continuous electric field evolution) and a sample temperature of 60 K was applied. 3D reconstruction and cluster identification by maximum separation method (with the aim to calculate the number density of clusters only) were performed using IVAS 3.6.14 software.

3 RESULTS AND DISSCUSSION

The DSC analysis performed on the Fe-9Cr specimen is displayed on Figure 1. The temperature Ac1 = 890 °C and Ac3 = 960 °C are reported on the graph. These two values are in good agreement with others performed on F/M ODS steels, which are known to display higher temperature of $\alpha \rightarrow \gamma$ transformation than non-strengthened F/M steels [10], [11].

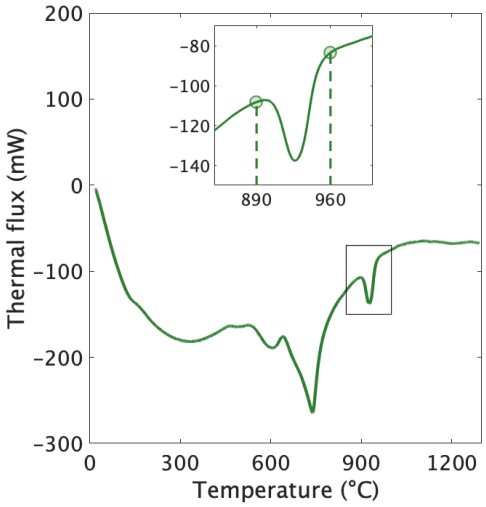

Figure 1: Evolution of the thermal flux from DSC test showing the $\alpha \rightarrow \gamma$ phase transformation between Ac1 = 890 °C and Ac3 = 960 °C on a Fe-9Cr ODS powder.

SAXS intensity curves all along the thermal treatment on the CP-14Cr and CP-9Cr samples and after HE for the HE-14Cr and HE-9Cr sample are presented in Figure 2. The curves on Figure 2a and a' represent the ESRF synchrotron in-situ acquisition. The curves on Figure 2b and b' are extracted from laboratory SAXS measurements, which explains the higher level of noise. For visibility purpose, those scattering curves were artificially shifted by a decade. From the comparison of the curves coming from the Fe-14Cr and those coming from the Fe-9Cr, a clear

difference can be seen at the most advanced annealing stages, as the CP/HE-9Cr looks to display bigger nano-oxides. Moreover, the scattering curves of all CP specimens at the as-MA stage display a scattering from very small object that demonstrates that the as-MA stage is not a fully homogeneous solid solution.

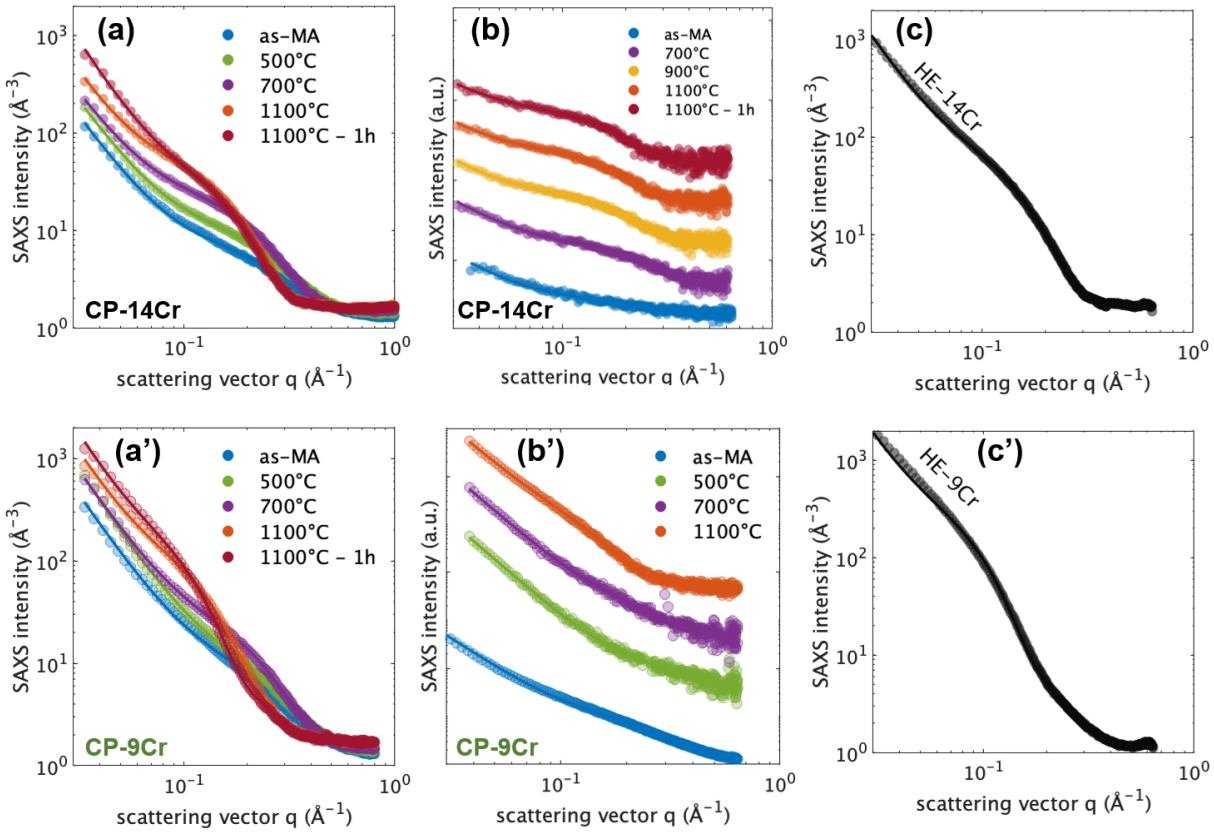

Figure 2: SAXS intensity curves at several temperatures during the in-situ heating on CP-14Cr (a), and CP-9Cr (a'), after several interrupted thermal treatment on the CP-14Cr (b), and on the CP-9Cr (b') and after HE on the HE-14Cr (c) and HE-9Cr (c').

From the previously presented scattering curves, the evolution of nano-oxides mean radius for the CP-14Cr and CP-9Cr is shown in Figure 3. The curve is plotted with respect to the temperature during the heating ramp and with respect to the holding time during the 1100°C isothermal. On this graph the Ac1 and Ac3 temperature had been reported as vertical red lines, indicating the beginning and the end of the $\alpha \rightarrow \gamma$ transformation on the CP-9Cr only, as the CP-14Cr remain purely α all along the thermal treatment. The mean radius on the HE-14Cr and HE-9Cr are also plotted at the end of the curve, and are very coherent with the final measurements performed on the CP samples, which tends to confirm the representativity of the heated CP samples regarding the HE industrial process.

Presence of very small as-MA clusters are confirmed on both CP-14Cr and CP-9Cr specimens. These clusters start growing at around 450°C, on both specimens. After Ac3, the CP-14Cr and CP-9Cr nano-oxides mean radius – previously almost perfectly identical – start to diverge from each other. This divergence, exactly occurring at the $\alpha \rightarrow \gamma$ transformation temperature, allows to link with a quasi-certitude the precipitation kinetics change to the matrix phase transformation on the Fe-9Cr ODS steels. The growth rate of CP-9Cr (in a γ matrix) becomes much higher than the CP-14Cr specimen (in an α matrix). During the isothermal, the coarsening of CP-9Cr nano-oxides is slight, but is clearly noticeable, where almost no coarsening can be observed on the CP-14Cr sample, even after 1 h at 1100°C. This extremely sluggish coarsening

makes the Y-Ti-O nano-oxides one of the most stable precipitates phase among precipitation-hardened alloy (even for F/M ODS, but especially for purely ferritic ODS). At the end of the CP thermal treatment (and also for the HE specimens) the final size on the F/M is approximately two times higher than on the purely ferritic, which is in good accordance with the literature [9]. This discrepancy in size would tend to induce a slower coarsening for the CP-9Cr nano-oxides (bigger) than on the CP-14Cr (smaller). Therefore, the higher coarsening observed in the CP-9Cr reveals the drastically different behaviour of the nano-oxides in a γ than in an α matrix.
The origin of this change of behaviour is still not fully understood, and a detailed analysis lays out of the scope of the present article. The principal hypothesis are:

(i) A difference in the interfacial energy, as the matrix passes from α Body Centred Cubic (BCC) structure to γ Face Centred Cubic (FCC) structure.

(ii) A loss of the coherent relationship between the nano-oxides and the matrix, which could also cause an increase of the interfacial energy on F/M ODS steels, and then a higher coarsening.

(iii) A difference in the diffusion coefficient and solubility limit of Y, Ti and O after the $\alpha \rightarrow \gamma$ phase transformation of the matrix, which could significantly influence the precipitation kinetics as well.

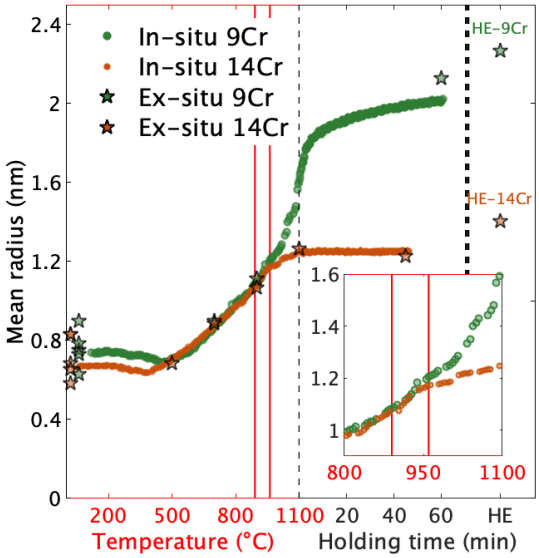

Figure 3: Evolution of the mean radius of nano-oxides extracted from in- and ex-situ SAXS experiments on the CP-14Cr, CP-9Cr, HE-14Cr and HE-9Cr specimens.

Using APT, the clusters present at the as-MA stages can be clearly noticed, as displayed on the Figure 4 on the CP-14Cr as-MA sample. These as-MA clusters seems to display Y- and O-rich clusters at least with a potential presence of Ti-enrichment as well. It should be noted however that no size evaluation can be performed from APT data, as reconstruction artefacts are known to very significantly modify the apparent cluster size on those alloys.

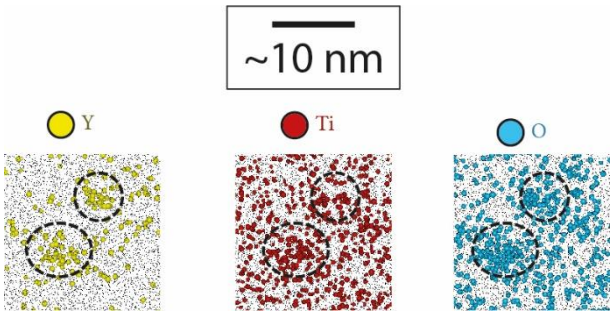

Figure 4: 3D reconstruction from APT measurements showing slices of around 10 nm thick of the Y, Ti and O, displaying two clusters on the CP-14Cr at the as-MA stage.

The evolution of $\Delta\rho^2 \times f_v$ is plotted on the Figure 5 for the CP-14Cr sample (Figure 5a), and for the CP-9Cr sample (Figure 5b). On this graph the two energies used for the measurements are displayed in light colors and dark color respectively for E1 = 16.829 keV and E2 = 17.009 keV. The gap present between the two energies used for the measurements, demonstrates the presence of Y inside the precipitates all along the thermal treatment, from the as-MA clusters (as already shown by APT in Figure 4) to the final Y-Ti-O oxides.

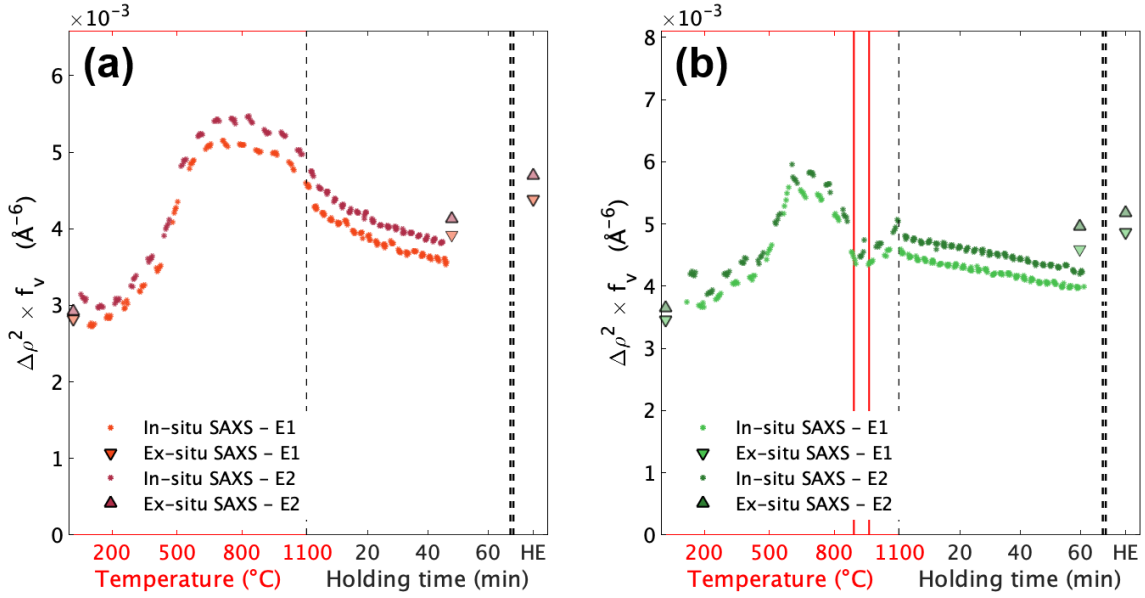

Figure 5: Evolution of the $\Delta\rho^2 \times f_v$ on the CP-14Cr (a), and CP-9Cr (b), at two levels of energies (E1 = 16.829 keV and E2 = 17.009 keV).

From the evolution of the SAXS $\Delta\rho^2 \times f_v$ and R_m it is possible to compute the evolution of the number density N which can be expressed as:

$$\mathrm{N} = \frac{f_v}{\frac{4}{3}\pi R_m^3} \tag{1}$$

The value of f_v can only be assessed from $\Delta\rho^2 \times f_v$ by making an assumption on the value of $\Delta\rho^2$ and thus, an assumption on the nano-oxides nature. Here, we choose to assume the nano-oxides as $Y_2Ti_2O_7$ pyrochlore all along the thermal treatment.

The SAXS number density can be compared to the APT number density determined by maximum separation method. This method do not rely on any hypothesis on the nano-oxide nature. Therefore, a discrepancy between the SAXS (calculated with the $Y_2Ti_2O_7$ pyrochlore assumption) and APT (measured from counting the clusters divided by the APT tip volume)

number densities reveals a bias into the hypothesis performed, and then, a nano-oxides nature different from $Y_2Ti_2O_7$ pyrochlore (chemical composition and/or structure).

The graph showing the comparison between those two number densities is presented in Figure 6. The significant gap (around one order of magnitude) from the as-MA stage to ~700 °C demonstrates that the precipitates are clearly not $Y_2Ti_2O_7$ (nor Y_2TiO_5, as this hypothesis would also have resulted in similar SAXS number density) at the beginning of the thermal treatment. After ~700 °C the gap reduce and become insignificant on both alloys around ~1000 °C. Thus, on the isothermal, the presence of $Y_2Ti_2O_7$ (or Y_2TiO_5) is confirmed for both alloys. It could also be noticed that the number density at the end of the thermal treatment for the CP-9Cr and HE-9Cr are lower than the number density displayed on the CP-14Cr and HE-14Cr, which is a direct result of the decrease of mean radius previously observed (at equal volume fraction of nano-oxides).

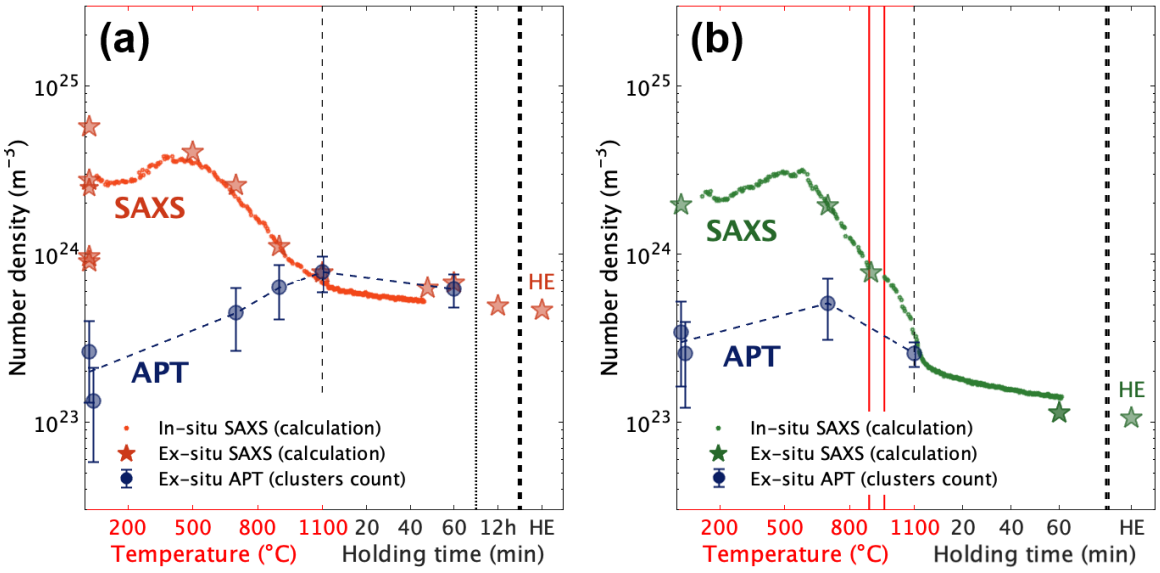

Figure 6: Evolution of the number density calculated by SAXS and measured by APT on the CP/HE-14Cr sample (a), and on the CP/HE-9Cr sample (b).

4 CONCLUSION

In the present article the difference in terms of precipitation evolution on F/M and purely ferritic ODS steels are assessed. A clear difference in the precipitation behaviour had been observed between the two alloys and results in a bigger nano-oxides size (~ 2 times), with a lower number density on the F/M ODS steel compared to the purely ferritic ODS steel. This difference can be linked to the phase transformation of the matrix as the precipitates properties are extremely similar from as-MA stage to the Ac3 temperature and diverge just afterward. On both alloy, a stabilisation of the nano-oxides structure and stoichiometry seems to occur around ~1000°C. Those findings can help the design of the F/M ODS steels process and be invaluable dataset for precipitation simulation models (for F/M and purely ferritic ODS steels).

ACKNOWLEDGMENTS

Authors strongly acknowledge Nathalie Boudet, Nils Blanc, Gilbert Chahine and Stephan Arnaud, the scientific team of D2AM- BM02 beamline of the ESRF synchrotron. This research is founded by the Reactors of 4th Generation (R4G) program of the French Alternative Energies

and Atomic Energy Commission (CEA). This work received assistance from the "Agence Nationale de la Recherche" program GENESIS referenced as ANR-11-EQPX-0020.

REFERENCES

[1] S. Ukai, S. Ohtsuka, T. Kaito, Y. de Carlan, J. Ribis, and J. Malaplate, *Oxide dispersion-strengthened/ ferrite-martensite steels as core materials for Generation IV nuclear reactors*. 2017.

[2] P. Yvon, M. L. Flem, C. Cabet, and J. L. Seran, "Structural materials for next generation nuclear systems: Challenges and the path forward," *Nuclear Engineering and Design*, vol. 294, pp. 161–169, 2015, doi: 10.1016/j.nucengdes.2015.09.015.

[3] M. Praud *et al.*, "Study of the deformation mechanisms in a Fe–14% Cr ODS alloy," *Journal of Nuclear Materials*, vol. 428, no. 1–3, pp. 90–97, Sep. 2012, doi: 10.1016/j.jnucmat.2011.10.046.

[4] M. Dadé *et al.*, "Influence of temperature and strain rate on the deformation and damage mechanisms of oxide dispersion strengthened ferritic steels," *Materialia*, vol. 4, pp. 585–594, Dec. 2018, doi: 10.1016/j.mtla.2018.11.016.

[5] T. Stan, Y. Wu, J. Ciston, T. Yamamoto, and G. R. Odette, "Characterization of polyhedral nano-oxides and helium bubbles in an annealed nanostructured ferritic alloy," *Acta Materialia*, vol. 183, pp. 484–492, Jan. 2020, doi: 10.1016/j.actamat.2019.10.045.

[6] P. Dubuisson, Y. de Carlan, V. Garat, and M. Blat, "ODS Ferritic/martensitic alloys for Sodium Fast Reactor fuel pin cladding," *Journal of Nuclear Materials*, vol. 428, no. 1–3, pp. 6–12, Sep. 2012, doi: 10.1016/j.jnucmat.2011.10.037.

[7] T. Tanno, M. Takeuchi, S. Ohtsuka, and T. Kaito, "Corrosion behavior of ODS steels with several chromium contents in hot nitric acid solutions," *Journal of Nuclear Materials*, vol. 494, pp. 219–226, 2017, doi: 10.1016/j.jnucmat.2017.07.008.

[8] E. Vakhitova, D. Sornin, F. Barcelo, and M. François, "Texture evolution in Oxide Dispersion Strengthened (ODS) steel tubes during pilgering process," *Journal of Nuclear Materials*, vol. 494, pp. 20–28, 2017, doi: 10.1016/j.jnucmat.2017.07.002.

[9] L. Toualbi *et al.*, "Assessment of a new fabrication route for Fe-9Cr-1W ODS cladding tubes," *Journal of Nuclear Materials*, vol. 428, pp. 47–53, 2012, doi: 10.1016/j.jnucmat.2011.12.013.

[10] M. Yamamoto, S. Ukai, S. Hayashi, T. Kaito, and S. Ohtsuka, "Formation of residual ferrite in 9Cr-ODS ferritic steels," *Materials Science and Engineering: A*, vol. 527, no. 16–17, pp. 4418–4423, Jun. 2010, doi: 10.1016/j.msea.2010.03.079.

[11] M. Yamamoto, S. Ukai, S. Hayashi, T. Kaito, and S. Ohtsuka, "Reverse phase transformation from α to γ in 9Cr-ODS ferritic steels," *Journal of Nuclear Materials*, vol. 417, pp. 237–240, 2011, doi: 10.1016/j.jnucmat.2010.12.250.

[12] G. Spartacus *et al.*, "Nano-oxide precipitation kinetics during the consolidation process of a ferritic oxide dispersion strengthened steel.," *Scripta Materialia*, vol. 188, pp. 10–15, Nov. 2020, doi: 10.1016/j.scriptamat.2020.07.003.

[13] M. Dumont, L. Commin, I. Morfin, F. Degeuser, F. Legendre, and P. Maugis, "Chemical composition of nano-phases studied by anomalous small-angle X-ray scattering: Application to oxide nano-particles in ODS steels," *Materials Characterization*, vol. 87, pp. 138–142, 2014, doi: 10.1016/j.matchar.2013.11.008.

[14] C. A. Williams, P. Unifantowicz, N. Baluc, G. D. W. Smith, and E. A. Marquis, "The formation and evolution of oxide particles in oxide-dispersion-strengthened ferritic steels during processing," *Acta Materialia*, vol. 61, pp. 2219–2235, 2013, doi: 10.1016/j.actamat.2012.12.042.